

Nonlinear electronic excitations in crystalline solids using meta-generalized gradient approximation and hybrid functional in time-dependent density functional theory

Shunsuke A. Sato,¹ Yasutaka Taniguchi,^{2,3} Yasushi Shinohara,⁴ and Kazuhiro Yabana^{1,2}

¹*Graduate School of Pure and Applied Sciences,
University of Tsukuba, Tsukuba 305-8571, Japan*

²*Center for Computational Science, University of Tsukuba, Tsukuba 305-8571, Japan*

³*Department of Medical and General Sciences, Nihon Institute of Medical Science,
1276 Shimogawara, Moroyama-machi, Iruma-gun, Saitama 350-0435, Japan*

⁴*Max Planck Institute of Microstructure Physics, 06120 Halle, Germany*

Abstract

We develop numerical methods to calculate electron dynamics in crystalline solids in real-time time-dependent density functional theory employing exchange-correlation potentials which reproduce band gap energies of dielectrics; a meta generalized gradient approximation (meta-GGA) proposed by Tran and Blaha [Phys. Rev. Lett. 102, 226401 (2009)] (TBm-BJ) and a hybrid functional proposed by Heyd, Scuseria, and Ernzerhof [J. Chem. Phys. 118, 8207 (2003)] (HSE). In time evolution calculations employing the TB-mBJ potential, we have found it necessary to adopt a predictor-corrector step for stable time-evolution. Since energy functional is not known for the TB-mBJ potential, we propose a method to evaluate electronic excitation energy without referring to the energy functional. Calculations using the HSE hybrid functional is computationally expensive due to the nonlocal Fock-like term. We develop a computational method for the operation of the Fock-like term in Fourier space, for which we employ massively parallel computers equipped with graphic processing units. To demonstrate significances of utilizing potentials providing correct band gap energies, we compare electronic excitations induced by femtosecond laser pulses using the TB-mBJ, HSE, and a simple local density approximation (LDA). At low laser intensities, electronic excitations are found to be sensitive to the band gap energy: results using TB-mBJ and HSE are close to each other, while the excitation of the LDA calculation is more intensive than the others. At high laser intensities close to a damage threshold, we have found that electronic excitation energies are similar among the three cases.

I. INTRODUCTION

At current frontiers of optical sciences, interactions of intense and ultra-short laser pulses with solids are attracting much interests [1–3]. For example, ultra-short laser pulses with intensities above a damage threshold are used for non-thermal laser-processing [4, 5]. Ultra-short laser pulses irradiated on dielectrics close to the damage threshold have been found to show intriguing phenomena such as producing an ultrafast charge transfer [6], and modifying the band gap in sub-femtosecond time scale [7]. These phenomena induced by ultra-short, intense laser pulses are expected to open up new technological applications.

For microscopic understanding of these phenomena, it is quite significant to theoretically investigate nonlinear electron dynamics in the medium excited by the strong electric field of laser pulses. Real-time calculation based on the time-dependent density functional theory (TDDFT) [8] is a useful theory for the investigation of nonlinear electron dynamics. It has been applied to nonlinear laser-solid interactions such as optical breakdown [9], generation of coherent phonon [10], and calculation of nonlinear optical properties [11], as well as linear responses for a weak field [12].

In order to apply the TDDFT to practical problems, we need to use approximate exchange-correlation potentials. In most applications of the TDDFT, adiabatic approximation, in which the exchange-correlation potential at each time is determined by the density (, current, and kinetic density if necessary) at the same time, is assumed. In the following developments, we will consider three exchange-correlation potentials: local density approximation (LDA), meta generalized gradient approximation (meta-GGA), and hybrid functional, and use them in both ground state and time evolution calculations in the adiabatic approximation.

Among the three approximations, the LDA is the simplest one. We will use the energy functional of Ref. [13]. Because of the well-known band gap problem in the static LDA calculations, optical gaps of semiconductors and insulators are also underestimated in the TDDFT using the adiabatic LDA. The underestimation of the optical gap causes serious problems when we compare calculated physical quantities with experimental results in nonlinear electronic excitations induced by intense laser pulses as well as in linear responses for a weak optical fields.

Recently, Tran and Blaha proposed a meta-GGA exchange potential which systematically

improves the band gap energy of various materials [14]. We abbreviate the potential as TB-mBJ potential. Calculated band gap energies using the TB-mBJ potential agree with experimental gap energies in a quality similar to those by the *GW* method [14].

Hybrid functional is, at present, one of the most successful approximations in practical applications of static and time-dependent density functional theory. In solid state physics, a hybrid functional that is proposed by the Heyd, Scuseria, and Ernzerhof (HSE) has been widely applied [15]. The HSE functional significantly improves fundamental gap comparing to one in the LDA. It has been shown that also accurate optical absorption spectra in several dielectrics and partial inclusion of excitonic excitation by J. Paier *et al* [16].

In this work, we present numerical methods to achieve time-evolution calculations in the real-time TDDFT employing the TB-mBJ and HSE potentials. We have already reported results employing the TB-mBJ potential in the real-time TDDFT for light-matter interactions in both linear and nonlinear regimes [17–19]. To carry out stable time-evolution calculations, we find that a predictor-corrector step is indispensable in the calculations using the TB-mBJ potential, while it is not necessary in the calculations using the LDA and HSE potentials. The TB-mBJ potential is given in Ref. [14] without referring to the energy functional, and an explicit form of the energy functional providing the TB-mBJ potential is not known. We discuss how to evaluate electronic excitation energies during the irradiation of a laser pulse without referring to the energy functional. In order to calculate nonlinear electron dynamics using the HSE functional, we develop a Fourier-space method for the Fock-like operations: the non-local Fock-like term in the HSE functional is calculated in Fourier space, making use of an efficient Fast-Fourier-Transformation library on an accelerator type super-computer. We apply the above methods for crystalline silicon under irradiation of ultrashort laser pulses, and compare electronic excitations by the three potentials.

The paper is organized as follows. In Sec. II, we describe methods of electron dynamics calculations in crystalline solids utilizing the TB-mBJ and HSE potentials. In Sec. III and IV, we present calculations for electron dynamics in crystalline silicon, using LDA, TB-mBJ, and HSE potentials in linear and nonlinear regimes, respectively. In Sec. V, a summary is presented.

II. FORMALISM

A. Electron dynamics calculation in crystalline solids

First we briefly explain a general feature of electron dynamics calculations in crystalline solids based on the TDDFT. Details of the method are explained in Ref. [12]. We consider electron dynamics in crystalline solids under visible or infrared laser pulses. A typical wavelength of the electric field of such laser pulses is a micrometer, while the length scale of the electron dynamics induced by the laser pulse is less than a nanometer. Therefore, in a unit cell of crystalline solids, we can treat the laser electric field as a spatially-uniform and time-dependent electric field $\vec{E}(t)$. This is a dipole approximation for interactions between the laser pulse and electrons in a medium. The electron dynamics is described by the following time-dependent Kohn-Sham (TDKS) equation,

$$i\hbar\frac{\partial}{\partial t}\psi_i(\vec{r}, t) = h_{KS}(t)\psi_i(\vec{r}, t), \quad (1)$$

where $h_{KS}(t)$ is the time-dependent Kohn-Sham Hamiltonian. It is given by

$$h_{KS}(t) = \frac{\{-i\hbar\vec{\nabla} + \frac{e}{c}\vec{A}(t)\}^2}{2m_e} + \hat{v}_{ion}[\vec{A}(t)] + v_H(\vec{r}, t) + v_{xc}(\vec{r}, t), \quad (2)$$

where $\vec{A}(t)$ is the vector potential which is related to the electric field $\vec{E}(t)$ by $\vec{A}(t) = -c \int^t dt' \vec{E}(t')$. The Hamiltonian contains the Hartree potential $v_H(\vec{r}, t)$, an exchange-correlation potential $v_{xc}(\vec{r}, t)$, and an ionic potential $\hat{v}_{ion}[\vec{A}(t)]$. The Hamiltonian of Eq. (2) is periodic in space so that we may apply the Bloch theorem to the orbitals $\psi_i(\vec{r}, t)$ at each time. For the ionic potential, we employ a norm-conserving pseudopotential [20] with the separable approximation [21]. The ionic potential depends on the vector potential $\vec{A}(t)$ due to the nonlocality of the potential [12].

The electric field $\vec{E}(t)$ may include an induced polarization field which depends on macroscopic geometry of the material which we treat. In the present calculation, we assume the transverse geometry explained in Ref. [22] in which the induced polarization fields do not appear. Moreover, the vector potential $\vec{A}(t)$ may include exchange-correlation terms in the time-dependent current density functional theory [23, 24]. We simply ignore them, since reliable potentials have not yet been available at present.

We define a matter current density of electrons $\vec{j}(\vec{r}, t)$,

$$\vec{j}(\vec{r}, t) = \frac{1}{m_e} \sum_i \Re \left[\psi_i^*(\vec{r}, t) \left\{ -i\hbar\vec{\nabla} + \frac{e}{c}\vec{A}(t) \right\} \psi_i(\vec{r}, t) \right]. \quad (3)$$

and spatially averaged electric current density $\vec{J}(t)$,

$$\vec{J}(t) = -e \frac{1}{\Omega} \int_{\Omega} \vec{j}(\vec{r}, t) d\vec{r} + \vec{J}_{NL}(t), \quad (4)$$

where Ω is a volume of the unit cell and $\vec{J}_{NL}(t)$ is a contribution from the nonlocal part of the ionic pseudopotential [12].

B. Exchange-correlation potentials

We will use the LDA, TB-mBJ, and HSE potentials in the real-time TDDFT calculations in the adiabatic approximation. We present below brief explanations for the TB-mBJ and HSE potentials.

The TB-mBJ exchange potential in the adiabatic approximation has the following form,

$$v_{TB-mBJ}^{ex}(\vec{r}, t) = c_m v_{BR}(\vec{r}, t) + (3c_m - 2) \frac{1}{\pi} \sqrt{\frac{5}{12}} \sqrt{\frac{\tau(\vec{r}, t)}{\rho(\vec{r}, t)}}, \quad (5)$$

where $v_{BR}(\vec{r}, t)$ is the Becke-Roussel potential [25], $\rho(\vec{r}, t) = \sum_i |\psi_i(\vec{r}, t)|^2$ is the electron density, and $\tau(\vec{r}, t)$ is the kinetic energy density given by

$$\tau(\vec{r}, t) = \frac{1}{m_e} \sum_i \left| \left\{ -i\hbar \vec{\nabla} + \frac{e}{c} \vec{A}(t) \right\} \psi_i(\vec{r}, t) \right|^2. \quad (6)$$

It has been known that the band gap depends crucially on the parameter c_m of Eq. (5) [26]. In the original TB-mBJ paper [14], a formula for the mixing parameter c_m is proposed using the electron density and its gradient. In this work, we treat the parameter c_m as adjustable and determine the value in such a way that the band gap coincides with the experimental gap of silicon. As will be shown, we may find the value of c_m that reproduces the experimental optical gap as well as the band gap simultaneously. The potential of Eq. (5) is not gauge invariant, since the kinetic energy density of Eq. (6) is not [27–30]. To recover the gauge invariance, we replace all kinetic energy density terms in the potential as

$$\tau(\vec{r}, t) \rightarrow \tau(\vec{r}, t) - \vec{j}^2(\vec{r}, t) / \rho(\vec{r}, t), \quad (7)$$

where $\vec{j}(\vec{r}, t)$ is the current density of Eq. (3). For the correlation potential, we use the PW91 correlation potential [31] following the original TB-mBJ paper [14].

The HSE exchange-correlation potential is given by

$$v_{xc} = v_{xc}^{PBE} - \frac{1}{4} v_x^{SR,PBE} + \frac{1}{4} \hat{v}^{SR,Fock}, \quad (8)$$

where v_{xc}^{PBE} is the PBE exchange-correlation potential [32], $v_x^{SR,PBE}$ and $v^{SR,Fock}$ are the PBE exchange and the non-local Fock-like potentials corresponding to the short-range part of the Coulomb potential. The HSE exchange-correlation potential includes a parameter μ , the range separation parameter for the Coulomb interaction. In this work, we use the value μ of 0.3 \AA^{-1} .

C. Numerical method

We solve the TDKS equation, Eq. (1), in real time and real space [33, 34]. We choose a cubic unit cell containing eight silicon atoms and 32 valence electrons in total. We consider electron dynamics only, freezing atomic positions at their equilibrium positions in the ground state. The unit cell is discretized by 16^3 uniform grid points. The first Brillouin zone is discretized by 24^3 k -points for calculations using the LDA and TB-mBJ potentials, and 12^3 k -points when using the HSE potential. We use the pseudopotential which was constructed using the LDA.

1. Predictor-corrector procedure

For time-evolution calculations, we repeat a time evolution of a small time step Δt :

$$\psi_i(\vec{r}, t + \Delta t) \approx \exp \left[\frac{h_{KS}(t + \frac{\Delta t}{2})}{i\hbar} \Delta t \right] \psi_i(\vec{r}, t), \quad (9)$$

where the Hamiltonian is approximately evaluated at a time $t + \Delta t/2$. We expand the time evolution operator, $\exp \left[h_{KS}(t + \frac{\Delta t}{2}) \Delta t / i\hbar \right]$, in Taylor series and take up to fourth order [33, 35]:

$$\exp \left[\frac{h_{KS}(t + \frac{\Delta t}{2})}{i\hbar} \Delta t \right] \approx \sum_{n=0}^4 \frac{1}{n!} \left(\frac{h_{KS}(t + \frac{\Delta t}{2})}{i\hbar} \Delta t \right)^n. \quad (10)$$

In the above procedure, we need to guess the Hamiltonian at a time $t + \Delta t/2$. In calculations using the LDA and HSE potentials, we find that use of the Hamiltonian at time t , $h_{KS}(t + \Delta t/2) \sim h_{KS}(t)$, provides results with sufficient accuracy. However, we have found that the predictor-corrector procedure to approximately evaluate $h_{KS}(t + \Delta t/2)$ is indispensable for stable time-evolution when we employ the TB-mBJ potential. The predictor-corrector procedure is usually carried out in the following steps [36]. We first calculate wave

functions $\psi_i^{pred}(\vec{r}, t + \Delta t)$ using the Hamiltonian at time t ,

$$\psi_i^{pred}(\vec{r}, t + \Delta t) = \exp \left[\frac{h_{KS}(t)\Delta t}{i\hbar} \right] \psi_i(\vec{r}, t). \quad (11)$$

Using the Kohn-Sham orbitals ψ_i^{pred} , we next construct the Hartree potential v_H^{pred} and the exchange correlation potential v_{xc}^{pred} at time $t + \Delta t$. We then approximate the Hamiltonian at time $t + \Delta t/2$ by averaging the potentials at time t and $t + \Delta t$ as follows:

$$v_H(\vec{r}, t + \frac{\Delta t}{2}) \approx \frac{v_H^{pred}(\vec{r}, t + \Delta t) + v_H(\vec{r}, t)}{2}, \quad (12)$$

$$v_{xc}(\vec{r}, t + \frac{\Delta t}{2}) \approx \frac{v_{xc}^{pred}(\vec{r}, t + \Delta t) + v_{xc}(\vec{r}, t)}{2}. \quad (13)$$

Finally, we calculate the Kohn-Sham orbitals at $t + \Delta t$ by Eq. (5) using the Hamiltonian at time $t + \Delta t/2$.

In the following, we numerically demonstrate the necessity of the predictor-corrector procedure when the TB-mBJ potential is used. Figure 1 shows the electric current in the crystalline silicon as a function of time after an instantaneous weak distortion is applied at $t = 0$. A time step of $\Delta t = 0.04$ a.u. is used. Figure 1 (a) shows the electric current using the LDA potential, and (b) shows the electric current using the TB-mBJ potential. In both panels, red-solid lines show results using the predictor-corrector procedure, while green-dashed lines show results without using the predictor-corrector procedure. One sees that, while the calculations using the LDA potential give the same result regardless of whether the predictor-corrector procedure is used, the calculations using the TB-mBJ potential proceed stably only if the predictor-corrector step is used. Until $t = 0.8$ fs (about 800 time steps), the calculated electric currents with and without the predictor-corrector procedure coincide with each other. However, at $t = 0.8$ fs, the calculation without the predictor-corrector procedure starts to show unphysical oscillations. We carried out calculations with and without the predictor-corrector procedure for several time steps, $\Delta t = 0.02, 0.04$, and 0.08 a.u., and have found that results without the predictor-corrector procedure always fail showing unphysical oscillations after a certain number of iterations. Calculations using the predictor-corrector procedure give the same result for the three time steps. We thus conclude that the predictor-corrector procedure is indispensable for stable time-evolution of orbitals when using the TB-mBJ potential. In the calculations presented below, we use the predictor-corrector procedure when we employ the TB-mBJ potential.

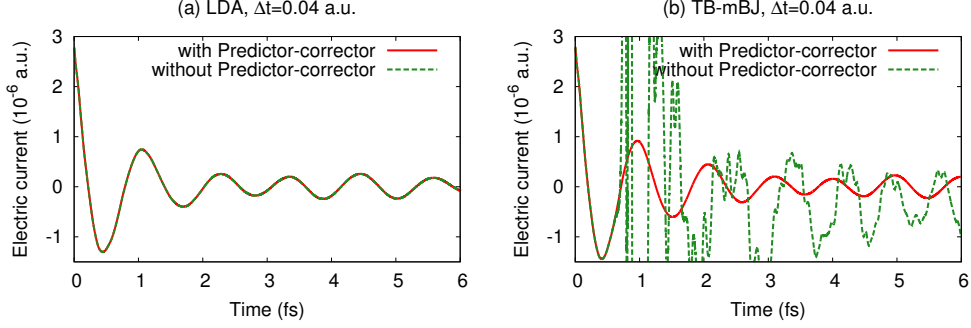


FIG. 1. (color online) Electric currents as functions of time after an instantaneous weak distortion is applied at $t = 0$. Panel (a) shows the results using the LDA potential, and panel (b) shows the results using the TB-mBJ potential. In both panels, calculated results with (red-solid) and without (green-dashed) the predictor-corrector procedure are compared.

2. Nonlocal Fock-like term

In calculations using the HSE potential, we need to calculate operations of nonlocal Fock-like term on orbitals. The nonlocal Fock-like term $\hat{v}^{SR,Fock}$ has the following form,

$$\hat{v}^{SR,Fock}\psi_i(\vec{r}, t) = \sum_{j=occ} \int d\vec{r}' v_{SR}(\vec{r} - \vec{r}') \psi_j(\vec{r}, t) \psi_j^*(\vec{r}', t) \psi_i(\vec{r}', t), \quad (14)$$

where only occupied orbitals are summed. $v_{SR}(\vec{r})$ is the short-ranged Coulomb-like potential, $v_{SR}(\vec{r}) = \text{erf}(\mu r)/r$. In practical calculations, we treat the nonlocal Fock-like term in Fourier space as:

$$\hat{v}^{SR,Fock}\psi_i(\vec{r}, t) = \sum_{j=occ} \psi_j(\vec{r}, t) \frac{1}{(2\pi)^3} \int d\vec{G} e^{-i\vec{G}\cdot\vec{r}} \tilde{v}^{SR}(\vec{G}) \tilde{\rho}_{ji}(\vec{G}, t), \quad (15)$$

where $\tilde{v}^{SR}(\vec{G})$ and $\tilde{\rho}_{ji}(\vec{G}, t)$ are Fourier transformation of $v^{SR}(\vec{r})$ and orbital products $\rho_{ji}(\vec{r}, t) = \psi_j^*(\vec{r}, t) \psi_i(\vec{r}, t)$, respectively.

The Fourier space operation has been carried out efficiently employing the Fast-Fourier-Transformation library on large-scale accelerator type supercomputers. In the HSE calculation, we further employ so-called down-sampling method [37] to reduce the computational cost, which we briefly describe below. First, we decompose the orbital index i into the reciprocal lattice vectors of the unit cell \vec{k} and the band index b : $\psi_i(\vec{r}, t) \rightarrow \psi_{\vec{k}b}(\vec{r}, t)$. Using this notation, we rewrite Eq. (15) as follows:

$$\hat{v}^{SR,Fock}\psi_{\vec{k}b}(\vec{r}, t) = \sum_{\vec{q}, b'=occ} \psi_{\vec{q}b'}(\vec{r}, t) \frac{1}{(2\pi)^3} \int d\vec{G} e^{-i\vec{G}\cdot\vec{r}} \tilde{v}^{SR}(\vec{G}) \tilde{\rho}_{\vec{q}b', \vec{k}b}(\vec{G}, t), \quad (16)$$

where the orbital product is described as $\rho_{\vec{q}b',\vec{k}b}(\vec{r},t) = \psi_{\vec{q}b'}^*(\vec{r},t)\psi_{\vec{k}b}(\vec{r},t)$ using the new indices. In the down-sampling method, the summation of Eq. (16) is carried out reducing the number of \vec{q} -points. In this work, we sample 12^3 k -points to describe Kohn-Sham orbitals, while we sample 4^3 q -points to evaluate the operation of the non-local Fock-like term of Eq. (16).

III. LINEAR RESPONSE CALCULATION IN REAL TIME

In this and next sections, we apply the real-time TDDFT calculations for electron dynamics in crystalline silicon using the LDA, TB-mBJ, and HSE potentials. Although linear response properties of solids may be investigated either in frequency or in time domains, time-domain calculation is a unique option for strongly nonlinear dynamics induced by ultra-short, highly-intense laser pulses. In this section, we discuss a real-time calculation for a dielectric function of silicon. The purpose of this section is to demonstrate that numerical methods of time evolution calculations presented in the previous section work stably in real-time linear response calculations.

For dielectric functions, several *ab-initio* approaches have been developed. Among them, *GW* plus Bethe-Salpeter equation approach [38, 39], which is based on many-body perturbation theory, has been successful to describe dielectric functions of various materials quantitatively. *Ab-initio* calculations based on TDDFT have also been presented [40]. Recently, dielectric functions in the TDDFT have been reported using meta-GGA [41] and HSE [16] functionals, which are successful in describing band gap energies of various materials correctly.

We briefly explain how we calculate dielectric function as a function of frequency in real-time TDDFT calculations. We calculate time evolution of electron orbitals under a weak electric field, $\vec{E}(t) = -\frac{1}{c}\frac{\partial}{\partial t}\vec{A}(t)$, solving Eq. (1). Using electric conductivity $\sigma_{ij}(t)$, the spatially-averaged electric current $\vec{J}(t)$, which is given by Eqs. (3) and (4), is related to the electric field $\vec{E}(t)$ by

$$J_i(t) = \sum_j \int dt' \sigma_{ij}(t-t')E_j(t'), \quad (17)$$

where i and j indicate Cartesian component, $i, j = x, y, z$. Taking Fourier transformations

of both sides, we obtain a relation in frequency representation,

$$J_i(\omega) = \sum_j \sigma_{ij}(\omega) E_j(\omega), \quad (18)$$

where $E_i(\omega)$, $J_i(\omega)$, and $\sigma_{ij}(\omega)$ are Fourier transformations of $E_i(t)$, $J_i(t)$, and $\sigma_{ij}(t)$, respectively. Frequency-dependent dielectric function $\epsilon_{ij}(\omega)$ is related to $\sigma_{ij}(\omega)$ as usual,

$$\epsilon_{ij}(\omega) = \delta_{ij} + \frac{4\pi i}{\omega} \sigma_{ij}(\omega). \quad (19)$$

In principle, we may use any electronic field $E_i(t)$ to calculate $\sigma_{ij}(\omega)$. For numerical convenience, we employ a δ -type distortion in z -direction for the electric field, $\vec{E}(t) = s\vec{e}_z\delta(t)$ where s is a small parameter. Then the conductivity is proportional to the electric current, $\sigma_{zz}(t) = J_z(t)/s$. This relation tells us that the Fourier transformation of the electric current provides the frequency-dependent conductivity. To reduce numerical noises caused by the finite evolution time T , we use a mask function $M(x)$ in the Fourier transformation as follows,

$$\sigma_{zz}(\omega) = \frac{1}{s} \int_0^T dt J_z(t) e^{i\omega t} M(t/T). \quad (20)$$

In practice, we employ the mask function $M(x) = 1 - 3x^2 + 2x^3$ [42].

Figure 2 shows electric currents $J_z(t)$ in crystalline silicon as functions of time after the delta-function distortion is applied at $t = 0$. Red-solid line shows the result using the HSE potential, green-dashed line shows the result using the TB-mBJ potential, and blue-dotted line shows the result using the LDA potential. All currents accurately coincide with each other at $t = 0$, since the initial current is determined by the sum rule [12]. Shortly after the distortion (0 fs to 1 fs), all currents look similar to each other. They start to depart after a few femtoseconds. As discussed above, the electric current is proportional to the conductivity as a function of time when we employ the delta-type distortion. Therefore, the difference of the currents directly reflects the difference of the conductivities.

From the currents shown in Fig. 2, dielectric functions can be calculated using Eqs. (19) and (20). Figure 3 shows the results: the real part in (a) and the imaginary part in (b). Red-solid line shows the result using the HSE potential, green-dashed line shows the result using the TB-mBJ potential, and blue-dotted line shows the result using the LDA potential. An experimental result [43] is also shown as black dash-dotted line. Our results using the HSE and TB-mBJ potentials shown in Fig. 3 almost coincide with previous calculations using frequency-domain methods [16, 41].

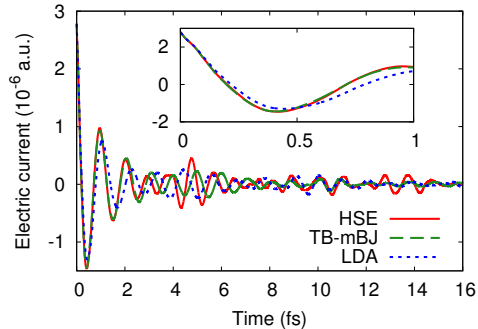


FIG. 2. (color online) Electric currents in crystalline silicon as functions of time after an impulsive distortion is applied at time $t = 0$. Results using the three exchange-correlation potentials are compared: HSE (red-solid), TB-mBJ (green-dashed), and LDA (blue-dotted).

As seen from the panel (b), the optical gap is underestimated when the LDA potential is used. This is closely related to the well-known band gap problem of the LDA. In contrast, the optical gap is well reproduced when we use the HSE and TB-mBJ potentials. The real parts of the dielectric functions calculated using the HSE and TB-mBJ potentials also reproduce accurately the experimental values in low frequency region (below 3 eV).

IV. NONLINEAR ELECTRON DYNAMICS UNDER INTENSE LASER PULSES

In this section, we investigate nonlinear electron dynamics in crystalline silicon under intense, ultra-short laser pulses using the three exchange-correlation potentials. We employ electric fields derived from the following vector potential,

$$A(t) = \begin{cases} -\frac{cE_0}{\omega} \cos(\omega t) \sin^2\left(\frac{\pi}{T_d}t\right) & (0 < t < T_d) \\ 0 & (\text{otherwise}), \end{cases} \quad (21)$$

where ω is a mean frequency of the field, T_d is the pulse duration, and E_0 is the maximum electric field of the pulse. We set ω and T_d to 1.35 eV/ \hbar and 16 fs, respectively. We define the maximum intensity of the laser pulse I_0 as $I_0 = cE_0^2/8\pi$. We calculate electron dynamics using three exchange-correlation potentials changing the intensity I_0 . We will examine two physical quantities: the excitation energy during and after the laser irradiation, and the number density of excited electrons after the laser irradiation.

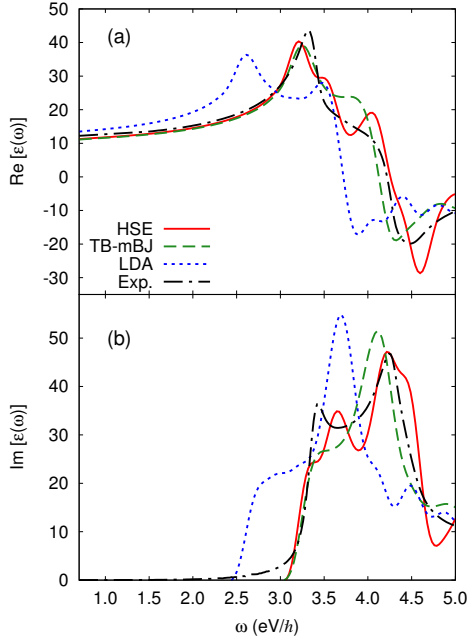


FIG. 3. Dielectric functions of silicon; real part in (a) and imaginary part in (b). Results using the three exchange-correlation potentials are compared: HSE (red-solid), TB-mBJ (green-dashed), and LDA (blue-dotted). An experimental result [43] is also shown as black-dash-dotted lines.

A. Excitation energy

We first consider electronic excitation energy induced by laser irradiation. The excitation energy is one of the most important quantities to investigate laser-matter interactions. For example, optical damage thresholds can be estimated by comparing the electronic excitation energy with cohesive energy of solids [44, 45]. Although the LDA and HSE potentials are explicitly derived from energy functionals, the TB-mBJ potential is not derived from any functionals but given directly. It is even unclear whether there exists an energy functional which provides the TB-mBJ potential. We first discuss how to evaluate electronic excitation energy when we use the TB-mBJ potential. We then investigate differences in electronic excitation energies using the three exchange-correlation potentials.

We first note that there are two procedures to calculate electronic excitation energy which should give the same results if the exchange-correlation potential is derived from an energy

functional. One is to use the explicit expression of the energy functional given by

$$E_{ex}(t) = \sum_i \int_{\Omega} d\vec{r} \psi_i^*(\vec{r}, t) \left[\frac{(-i\hbar\nabla + \frac{e}{c}\vec{A}(t))^2}{2m} + \hat{v}_{ion}[\vec{A}(t)] \right] \psi_i(\vec{r}, t) + \frac{1}{2} \int d\vec{r} v_H(\vec{r}, t) \rho(\vec{r}, t) + E_{xc}[\{\psi_i(\vec{r}, t)\}] - E_{GS}, \quad (22)$$

where E_{xc} is the exchange-correlation energy functional and E_{GS} is the energy of the ground state. The other is to calculate the work done on electrons by the laser electric field,

$$W(t) = \int_{-\infty}^t dt' \vec{J}(t') \cdot \vec{E}(t'), \quad (23)$$

where $\vec{J}(t)$ is the electric current defined by Eq. (4). When the exchange-correlation potential is derived from the energy functional $E_{xc}[\{\psi_i(\vec{r}, t)\}]$, we may easily prove that there holds

$$W(t) = \int_{-\infty}^t dt' \frac{d}{dt'} E_{ex}(t') = E_{ex}(t). \quad (24)$$

In calculations using the LDA and HSE potentials, we may employ either Eq. (22) or Eq. (23). In calculations using the TB-mBJ potential, Eq. (23) is the unique option.

Although Eq. (22) and Eq. (23) are analytically equivalent to each other if the potential is derived from an energy functional, we have found that Eq. (22) is numerically more favorable when the applied laser pulse is weak. Figure 4 shows $E_{ex}(t)$ of Eq. (22) using the LDA potential as a function of time for two intensities, $I = 1.0 \times 10^{10}$ W/cm² in (a) and $I = 1.0 \times 10^{13}$ W/cm² in (b). In the panel (a), we find an appreciable excitation energy during irradiation of the laser pulse. However, at the end of the pulse, the system almost returns to the ground state since the laser frequency is lower than the direct band gap. We shall call it *virtual* excitation. If we calculate the excitation energy using Eq. (23), the integrand $\vec{J}(t) \cdot \vec{E}(t)$ behaves oscillatory during the irradiation of the laser pulse. The integration over time mostly cancels and gives the total work done by the laser pulse which is very small as seen from the panel (a). Therefore, the calculation using Eq. (23) may suffer from an accumulation of a numerical error during the time integral. Figure 4 (c) compares the electronic excitation energies after the weak laser pulse ends ($I_0 = 1.0 \times 10^{10}$ W/cm²) using several different time steps Δt . Red up-pointing and green down-pointing triangles show the excitation energies calculated by Eq. (22) and by Eq. (23), respectively. As seen from the figure, results coincide numerically if we employ sufficiently small time step. The

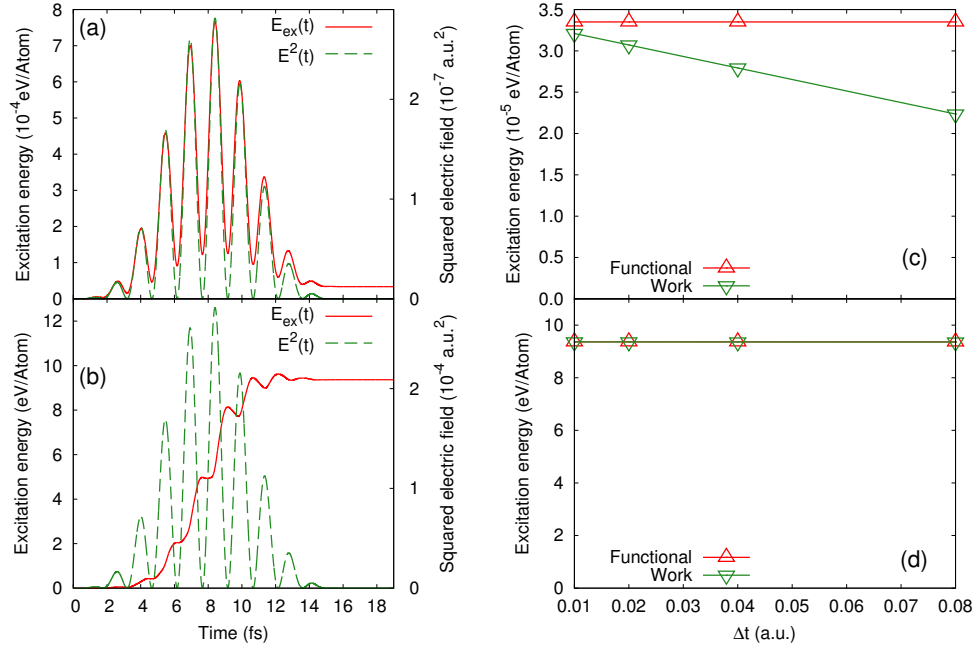


FIG. 4. Laser-induced electronic excitation energy calculated using the LDA potential. Panels (a) and (b) show the electronic excitation energy (red-solid) and the applied squared electric field (green-dashed) as functions of time. Panels (c) and (d) show the electronic excitation energy after the laser irradiation ends using Eqs. (22) and (23). Results in the panels (a) and (c) are for the irradiation of the weak laser pulse ($I_0 = 1.0 \times 10^{10} \text{ W/cm}^2$), while results in the panels (b) and (d) are for the irradiation of the strong laser pulse ($I_0 = 1.0 \times 10^{13} \text{ W/cm}^2$).

error in the excitation energy increases linearly with the time step Δt when we employ Eq. (23).

When the laser pulse is so strong that electrons are substantially excited by the laser pulse, we find a steady increase of the excitation energy in time, as seen in Fig. 4 (b). We shall call it *real* excitation. In this case, the difference in the numerical calculation is very small between the calculations using Eqs. (22) and (23), even if we employ the largest time step, $\Delta t = 0.08$ a.u.

When we use the TB-mBJ potential, we can only evaluate excitation energy using Eq. (23). To obtain excitation energy, we carry out two calculations using different time steps, $\Delta t = 0.02$ a.u. and $\Delta t = 0.01$ a.u. We then estimate the converged excitation energy by a linear extrapolation using the two calculations.

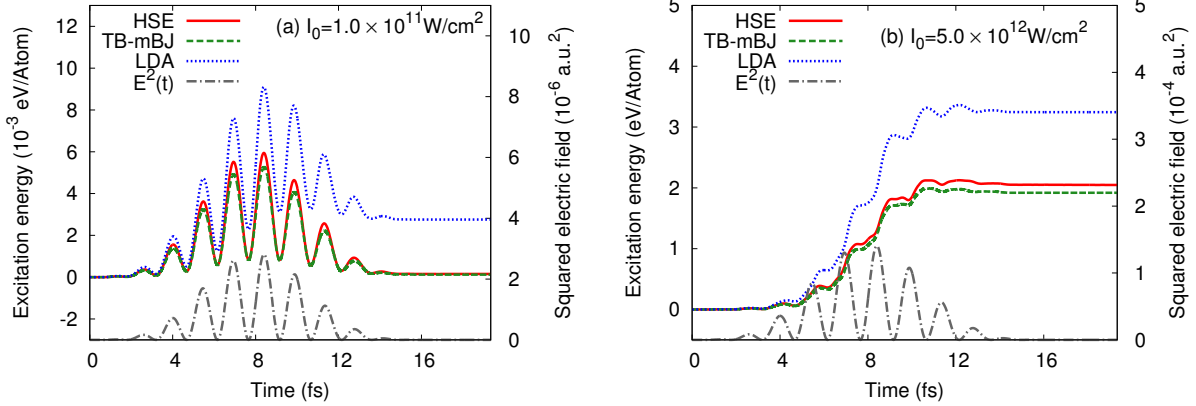


FIG. 5. (color online) Electronic excitation energies as functions of time induced by laser irradiation. Panel (a) shows the excitation energy under irradiation of a weak laser pulse ($I_0 = 1.0 \times 10^{11} \text{ W/cm}^2$), while panel (b) shows that of a strong laser pulse ($I_0 = 5.0 \times 10^{12} \text{ W/cm}^2$). Results using the three exchange-correlation potentials are compared: HSE (red-solid), TB-mBJ (green-dashed), and LDA (blue-dotted). Squared electric fields are also shown as gray-dash-dotted lines.

Figure 5 shows electronic excitation energies as functions of time using the three exchange-correlation potentials; LDA, TB-mBJ, and HSE. Figure 5 (a) shows results for a weak laser pulse ($I_0 = 1.0 \times 10^{11} \text{ W/cm}^2$), and Figure 5 (b) shows results for a strong laser pulse ($I_0 = 5.0 \times 10^{12} \text{ W/cm}^2$). Squared electric fields $E^2(t)$ are also shown as gray dash-dot lines in each panel. As seen from Fig. 5 (a), the electric field induces virtual excitation during the laser irradiation. After the irradiation ends, the excitation energies using the HSE and TB-mBJ potentials return to almost zero. In contrast, the excitation energy using the LDA potential remains finite after the irradiation, showing a substantial real excitation. These results indicate that wider optical gap in the calculations using the TB-mBJ and HSE potentials suppresses the real excitation (see Fig. 3).

Figure 5 (b) shows that electronic excitations induced by the strong electric field persist even after the pulse ends irrespective of the exchange-correlation potentials. One sees that the excitation energies using the HSE and TB-mBJ potentials are similar to each other, while the excitation energy using the LDA potential is larger than the others at each time. This is consistent with the above finding that the wider band gap suppresses the real excitation.

Next we investigate the electronic excitation energy after laser pulses end, changing the laser intensity I_0 . Figure 6 shows excitation energies after the pulses end ($t = 19.3 \text{ fs}$). Red

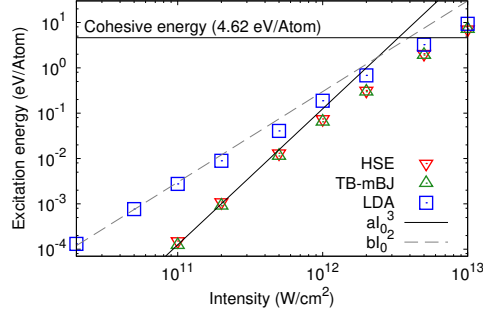


FIG. 6. (color online) Excitation energies as functions of laser intensity calculated using the three exchange-correlation potentials: HSE (red down-pointing triangle), TB-mBJ (green up-pointing triangle), and LDA (blue square). Cubed and squared intensities normalized to the excitation energies at low intensity are also shown as black-solid and gray-dashed lines, respectively.

down-pointing triangle shows the HSE result, green up-pointing triangle shows the TB-mBJ result, and blue square shows the LDA result. Lines of cubed and squared intensity of the laser pulses are also shown as black-solid and gray-dashed lines, respectively. These lines are normalized at low intensity to coincide with the excitation energies. Black horizontal line shows the cohesive energy of silicon, 4.62eV/atom [46], which may be regarded as a reference of the damage threshold.

Multi-photon excitations are expected for weaker intensities, while tunneling excitations are expected for stronger intensities [47]. At low intensity region, the excitation energy using the LDA potential can be fit with the squared intensity line I_0^2 , while the excitation energies calculated using the TB-mBJ and HSE potentials can be fit with the cubed intensity line I_0^3 . These behaviors indicate that two and three-photon absorption processes take place at the low intensity region for the LDA and the others cases, respectively. The numbers of absorbed photons are consistent with the ratio of the photon energy of the laser pulse ($\hbar\omega = 1.35$ eV) to the optical gap: the optical gap of silicon is 2.5 eV in the LDA case, and it is 3.1 eV in the HSE and the TB-mBJ cases (see Fig. 3).

One sees that the excitation energy using the LDA potential is much higher than the excitation energies using the HSE and TB-mBJ potentials at low intensity region. In contrast, the difference among the excitation energies becomes relatively small at high intensity region close to the cohesive energy of the medium.

B. Number density of excited electrons

The number density of excited electrons due to applied electric fields is one of significant observables to characterize laser excitation processes [48, 49]. To define the number density of excited electrons after laser irradiation, we first define eigenstates of the Kohn-Sham Hamiltonian after the laser pulse ends ($t_f = 19.3\text{fs}$),

$$h_{KS}(t_f)\phi_i(\vec{r}, t_f) = \epsilon_i^{t_f}\phi_i(\vec{r}, t_f). \quad (25)$$

Using these eigenstates, we define the number density of excited electrons n_{ex} by,

$$n_{ex} = n_{elec} - \frac{1}{\Omega} \sum_{i,j=occupied} |\langle \phi_i(t_f) | \psi_j(t_f) \rangle|^2, \quad (26)$$

where n_{elec} is the number density of valence electrons in the ground state, Ω is the volume of the unit cell, and $\psi_i(\vec{r}, t)$ are the time-dependent Kohn-Sham orbitals, which are solutions of Eq. (1). Only occupied states are summed in Eq. (26).

Figure 7 shows the number density of excited electrons as functions of laser intensity I_0 . We find similar features to those seen in excitation energies shown in Fig. 6. The number density using the HSE potential is very close to the number density using the TB-mBJ potential. The number density using the LDA potential is larger than the others. While the number density using the LDA potential is proportional to the squared intensity of laser pulse in the low intensity region, the number densities using the HSE and TB-mBJ potentials are proportional to the cubed intensity. At high intensity region, the number densities of excited electrons using three exchange-correlation potential are similar to each other.

Figure 8 shows excitation energy per excited electron, namely, the excitation energy shown in Fig. 6 divided by the number of excited electrons shown in Fig. 7 as a function of laser intensity I_0 . Twice and three times of the photon energy, 1.35 eV, are also shown by horizontal lines. At low intensity region, the excitation energy per excited electron using the TB-mBJ and HSE potentials approach to three times of the photon energy, 3×1.35 eV, while that using the LDA potential approaches twice of the photon energy, 2×1.35 eV. This fact obviously indicates that two and three-photon absorption processes dominate in the LDA case and the other cases, respectively, and is consistent with the intensity dependences seen in Figs. 6 and 7.

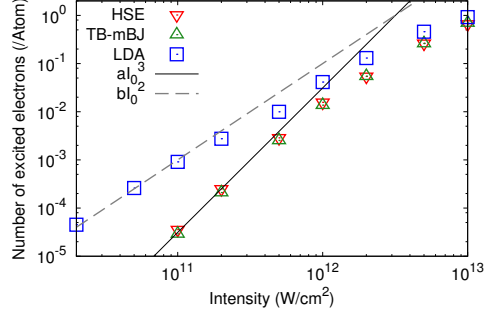


FIG. 7. (color online) The number densities of excited electrons as functions of laser intensity calculated using the three exchange-correlation potentials: HSE (red down-pointing triangle), TB-mBJ (green up-pointing triangle), and LDA (blue square). Cubed and squared intensities normalized to the number densities of excited electrons at low intensity are also shown as black-solid and gray-dashed lines, respectively.

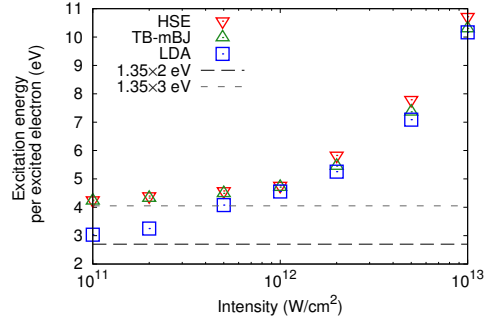


FIG. 8. (color online) Excitation energy per excited electron is plotted against the laser intensity calculated using the three exchange-correlation potentials: HSE (red down-pointing triangle), TB-mBJ (green up-pointing triangle), and LDA (blue square). Two horizontal lines are shown at 2×1.35 (black-dashed) and 3×1.35 eV (gray-dotted).

V. SUMMARY

In this paper, we developed methods to carry out real-time TDDFT calculations using the TB-mBJ meta-GGA potential and the HSE hybrid functional, which are known to reasonably reproduce band gaps of insulators. To carry out stable time evolution of orbitals using the TB-mBJ potential, we found that the predictor-corrector procedure is indispensable.

Without the predictor-corrector procedure, the electric current induced by an impulsive excitation shows unphysical oscillations after the time evolution of a few femtoseconds. This failure cannot be avoided even if we employ very small time step. In the calculations using hybrid functional, we developed a Fourier-space method to operate Fock-like term of hybrid functional on Kohn-Sham orbitals, making use of recently developed accelerator-type supercomputers.

We examined electron dynamics using the TB-mBJ, HSE, and LDA potentials. In linear response calculations, we investigated the dielectric response of crystalline silicon in time-domain. Calculated dielectric functions using the HSE and TB-mBJ potentials are confirmed to be similar to the previous results of frequency-domain TDDFT calculations [16, 41]. In electron dynamics calculations under strong, ultra-short laser pulses, we investigated the excitation energy and the number density of excited electrons during and after the laser irradiations. Since an explicit form of the energy functional corresponding to the TB-mBJ potential is not known, we developed a method to evaluate electronic excitation energy, not referring to the energy functional but calculating a work done by the external field to electrons. For irradiation of weak laser pulses, results using the HSE and TB-mBJ potentials are almost the same to each other, while the excitation energy and the number density of excited electrons of the LDA calculation are much larger than the others. For irradiation of strong laser pulses close to the damage threshold, we found that results are similar among the three potentials.

We consider that real-time TDDFT calculations using sophisticated exchange-correlation potentials such as the TB-mBJ and HSE potentials, which describe the band gap of various insulators reasonably, will enable us to carry out quantitative descriptions for electron dynamics in crystalline solids even under extremely nonlinear conditions. They are expected to provide significant insights and knowledge in wide fields of optical sciences including nonlinear optical responses, optical-control of electrons, and laser processing in solids.

ACKNOWLEDGMENTS

S.A.S thanks K. Sekizawa and G. Wachter for helpful discussion. This work is supported by the Japan Society of the Promotion of Science (JSPS) Grants-in-Aid for Scientific Research Grant Nos. 15H03674 and 25800124, and by the JSPS Grants-in-Aid for JSPS Fellows

Grant No. 26-1511. The numerical calculations were performed on the supercomputer at the Institute of Solid State Physics, University of Tokyo, T2K-Tsukuba and HA-PACS at the Center for Computational Sciences, University of Tsukuba.

- [1] T. Brabec and F. Krausz, *Rev. Mod. Phys.* **72**, 545 (2000).
- [2] G. A. Mourou, T. Tajima, and S. V. Bulanov, *Rev. Mod. Phys.* **78**, 309 (2006).
- [3] F. Krausz and M. Ivanov, *Rev. Mod. Phys.* **81**, 163 (2009).
- [4] M. D. Perry, B. C. Stuart, P. S. Banks, M. D. Feit, V. Yanovsky, and A. M. Rubenchik, *J. Appl. Phys.* **85**, 6803, (1999).
- [5] P. Balling and J. Schou, *Rep. Prog. Phys.* **76**, 036502 (2013).
- [6] A. Schiffrin, *et al*, *Nature* **493**, 70 (2013).
- [7] M. Schultze, K. Ramasesha, C.D. Pemmaraju, S.A. Sato, D. Whitmore, A. Gandman, J. S. Prell, L. J. Borja, D. Prendergast, K. Yabana, D. M. Neumark, and Stephen R. Leone *Science* **346**, 1348 (2014).
- [8] E. Runge and E. K. U. Gross, *Phys. Rev. Lett.* **52**, 997 (1984).
- [9] T. Otobe, M. Yamagiwa, J.-I. Iwata, K. Yabana, T. Nakatsukasa, and G. F. Bertsch, *Phys. Rev. B* **77**, 165104 (2005).
- [10] Y. Shinohara, K. Yabana, Y. Kawashita, J.-I. Iwata, T. Otobe, and G. F. Bertsch, *Phys. Rev. B* **82**, 155110 (2010).
- [11] V. A. Goncharov, *J. Chem. Phys.* **139**, 084104 (2013).
- [12] G. F. Bertsch, J.-I. Iwata, Angel Rubio, and K. Yabana, *Phys. Rev. B* **62**, 7998 (2000).
- [13] J. P. Perdew and A. Zunger, *Phys. Rev. B* **23**, 5048 (1981).
- [14] F. Tran and P. Blaha, *Phys. Rev. Lett.* **102**, 226401 (2009).
- [15] J. Heyd, G. E. Scuseria, and M. Ernzerhof, *J. Chem. Phys.* **118**, 8207 (2003).
- [16] J. Paier, M. Marsman, and G. Kresse, *Phys. Rev. B* **78**, 121201(R) (2008).
- [17] S. A. Sato, K. Yabana, Y. Shinohara, T. Otobe, and G.F. Bertsch, *Phys. Rev. B* **89**, 064304 (2014).
- [18] S.A. Sato, Y. Shinohara, T. Otobe, and K. Yabana, *Phys. Rev. B* **90**, 174303 (2014).
- [19] G. Wachter, C. Lemell, J. Burgdörfer, S. A. Sato, X. M. Tong, and K. Yabana, *Phys. Rev. Lett.* **113**, 087401 (2014).

- [20] N. Troullier and J. L. Martins, Phys. Rev. B **43**, 1993 (1991).
- [21] L. Kleinman and D. M. Bylander, Phys. Rev. Lett. **48**, 1425 (1982).
- [22] K. Yabana, T. Sugiyama, Y. Shinohara, T. Otobe, and G. F. Bertsch, Phys. Rev. B, **85**, 045134 (2012).
- [23] G. Vignale and W. Kohn, Phys. Rev. Lett. **77**, 2037 (1996).
- [24] J. A. Berger, P. L. de Boeij, and R. van Leeuwen, Phys. Rev. B **75**, 035116 (2007).
- [25] A. D. Becke and M. R. Roussel, Phys. Rev. A **39**, 3761, (1989).
- [26] D. Koller, F. Tran, and P. Blaha, Phys. Rev. B **85**, 155109 (2012).
- [27] J. Tao, Phys. Rev. B **71**, 205107 (2005).
- [28] J. Tao and J. P. Perdew, Phys. Rev. Lett. **95**, 196403 (2005).
- [29] S. Pittalis, E. Räsänen, and E. K. U. Gross, Phys. Rev. A **80**, 032515 (2009).
- [30] E. Räsänen, S. Pittalis, and C. R. Proetto, J. Chem. Phys. **132**, 044112 (2010).
- [31] J. P. Perdew and Y. Wang, Phys. Rev. B **45**, 13244 (1992).
- [32] J. P. Perdew, K. Burke, and M. Ernzerhof, Phys. Rev. Lett. **77**, 3865 (1996).
- [33] K. Yabana and G. F. Bertsch, Phys. Rev. B **54**, 4484 (1996).
- [34] I. Vasiliev, S. Ogut, and J.R. Chelikowsky, Phys. Rev. Lett. **82**, 1919 (1999).
- [35] H. Flocard, S. E. Koonin and M. S. Weiss, Phys. Rev. C **17**, 1682 (1978).
- [36] M. Walter, H. Häkkinen, L. Lehtovaara, M. Puska, J. Enkovaara, C. Rostgaard and J. J. Mortensen, J. Chem. Phys. **128**, 244101 (2008).
- [37] J. Paier, M. Marsman, K. Hummer, G. Kresse, I. C. Gerber, and J. G. Ángyán, J. Chem. Phys. **124**, 154709 (2006).
- [38] M. Rohlfing and S. G. Louie, Phys. Rev. Lett. **80**, 3320 (1998).
- [39] M. Rohlfing and S. G. Louie, Phys. Rev. B **62**, 4927 (2000).
- [40] G. Onida, L. Reining, and A. Rubio, Rev. Mod. Phys. **74**, 601 (2002).
- [41] V. U. Nazarov and G. Vignale, Phys. Rev. Lett. **107**, 216402 (2011).
- [42] K. Yabana, T. Nakatsukasa, J.-I. Iwata, and G. F. Bertsch, Phys. Status Solidi B **243**, 1121 (2006).
- [43] E. D. Palik, Handbook of Optical Constants of Solids (Academic Press, New York, 1985).
- [44] K.-M. Lee, C. M. Kim, S. A. Sato, T. Otobe, Y. Shinohara, K. Yabana, and T. M. Jeong, J. Appl. Phys. **115**, 053519 (2014).

- [45] S.A. Sato, K. Yabana, Y. Shinohara, T. Otake, K.M. Lee, and G.F. Bertsch, arXiv:1412.1445 [cond-mat.mtrl-sci].
- [46] B. Farid and R. W. Godby, Phys. Rev. B **43**, 14248 (1991).
- [47] L. V. Keldysh, Sov. Phys. JETP 20, 1307 (1965); J. Exp. Theor. Phys. (USSR) 47, 1945 (1964).
- [48] K. Sokolowski-Tinten and D. von der Linde, Phys. Rev. B **61**, 2643 (2000).
- [49] V. V. Temnov, K. Sokolowski-Tinten, P. Zhou, A. El-Khamhawy, and D. von der Linde, Phys. Rev. Lett. **97**, 237403 (2006).